



# Role of Sm dopant on structural, optical and efficient visible light photocatalytic performance of CdS nanoparticles by using simple wet chemical route

N. Jeevanantham<sup>1</sup> · O. N. Balasundaram<sup>1</sup>

Received: 12 April 2018 / Accepted: 21 June 2018  
© Springer Science+Business Media, LLC, part of Springer Nature 2018

## Abstract

The present work reported the samarium (Sm) doped CdS nanostructures synthesized via using co-precipitation method from cadmium and sulphide particle arrangements with no ligands at different temperature arrangement and amalgamation time. Structural, compositional, valance state and optical properties of the prepared samples were investigated using X-ray powder diffraction (XRD), transmission electron microscope (TEM/EDS mapping), X-ray photoelectron, Fourier transform infrared red, UV–Vis absorption and photoluminescence spectroscopes. XRD and TEM results suggest that Sm doped CdS samples were cubic structure with spherical shaped morphology with average diameter of around 14–28 nm. The prepared Sm doped CdS nanoparticles showed the superior photocatalytic activity for the degradation of RhB under visible light ( $\lambda > 420$  nm) irradiation, and 15 mol% Sm-doped CdS was found to be highly efficient for organic pollutants RhB and MB removal. Moreover, this catalyst showed improved stability, and the activity did not decrease significantly after seven recycles. This could be attributed to creation of electron–hole pairs and inhibit their recombination process by Sm doping. The improved mechanism by Sm doping is also discussed in detail.

## 1 Introduction

In recent years, many researchers have paid much attention in environmental pollution and energy utilization by using semiconductor photocatalyst. Semiconductor photocatalysts have a potential to exploit solar energy to solve many related problems, such as organic pollutants degradation, H<sub>2</sub> production from water splitting and waste water treatment [1–3]. An ideal photocatalyst require convenient synthesis of nanocrystal size and shape, thus allowing for improving their activity [4–7]. Because of the high light-harvesting efficiency, fast mobility of charge carriers, and superior catalytic activity [8, 9]. Among the different II–VI semiconductor group materials, cadmium sulfide (CdS) has got enormous concern in the observations and scientific community because of their wide band gap, high electron affinity and high photoconductivity. It has wide potential applications in electronics, optics, catalysis, and ceramics. These

applications are strongly contingent on the size, shape and component. CdS also has good photocatalytic activity due to its suitable band gap and fine optical transmittance [10, 11]. In recent years, several authors have working and improving the photocatalytic performance of CdS by using structure design or surface modification through different nanostructures such as nonorods, nanowires, nanobelts, quantum dots and nanospheres. nanospheres. But it was not fulfilling the attainment for increasing both the photoactivity and stability.

Metal ions doping (such as Zn, Ni, Co and Sm, etc.) is one of the effective and alternative method to controlling the band gap and absorption properties, which influence the photocatalytic properties of CdS. Generally, samarium ions (Sm<sup>3+</sup>) provide significant advantages to CdS, which modify the electronic structure and band gap of the CdS and improving the visible light absorption properties of CdS. Previously it was reported that samarium (Sm<sup>3+</sup>) ion increased the visible light absorption ability of TiO<sub>2</sub> and ZnO nanostructures for excellent photocatalytic activity [12, 13]. Hence, we report the preparation of Sm doped CdS nanocrystals by the chemical co-precipitation method and study the structural, optical and photocatalytic properties. To the best of the author's knowledge this is the first preliminary report about

✉ O. N. Balasundaram  
balupsg02@gmail.com

<sup>1</sup> Department of Physics, PSG College of Arts and Science, Coimbatore, Tamilnadu 641 014, India

structural, optical and photocatalytic properties of Sm doped CdS nanoparticles by simple wet chemical route.

## 2 Experimental procedure

### 2.1 Materials

Cadmium acetate dehydrate  $\text{Cd}(\text{CH}_3\text{COO})_2 \cdot 2\text{H}_2\text{O}$ , sodium sulfide ( $\text{Na}_2\text{S} \cdot 2\text{H}_2\text{O}$ ), samarium nitrate hexahydrate ( $\text{Sm}(\text{NO}_3)_3 \cdot 6\text{H}_2\text{O}$ ) for source materials for CdS and Sm respectively. The chemicals were purchased from Merk, India. All the chemicals used were of analytical grade and were used as received without any further purification.

### 2.2 Preparation of Sm doped CdS

High quality  $\text{Sm}^{3+}$  doped CdS nanoparticles were prepared by chemical precipitation method. In a typical synthesis, aqueous solution of 1.305 g of 0.1 M cadmium acetate dehydrate  $\text{Cd}(\text{CH}_3\text{COO})_2 \cdot 2\text{H}_2\text{O}$  and 0.1 M of  $\text{Sm}(\text{NO}_3)_3 \cdot 6\text{H}_2\text{O}$  was prepared separately. The concentration of Sm is varied from 5 to 15 mol%. Aqueous 0.1 M  $\text{Na}_2\text{S}$  solution was also prepared. Drop wise addition of  $\text{Na}_2\text{S}$  solution was then added slowly into the mixture of samarium nitrate and cadmium acetate solution with constant stirring. To this mixture, 20 ml of ethanol was further added and allowed for 6 h stirring. The  $\text{NH}_4\text{OH}$  (as precipitate agent) solution was added drop wise until the pH value reaches to 11. During this process the drop rate must be controlled in order to maintain the chemical homogeneity. The entire solution turned into yellowish orange in color and further allowed to stirrer for 48 h which in optimized aging period of the growth process. The dark green final products were washed thoroughly with the organic solvents (acetone, ethanol) and dried at 60 °C in a hot air oven and preserved in moisture free container. The pure CdS nanoparticles were prepared in a similar manner without use of Sm source.

### 2.3 Characterization techniques

The structure and average grain size of the samples were analyzed by using X-ray patterns of the powders were recorded using a Bruker D8-ADVANCE diffractometer (Cu  $K\alpha$  radiation:  $\lambda = 1.5418 \text{ \AA}$ ). TEM was recorded with JEM2100 model. High resolution electron microscope was recorded with accelerating voltage of 200 kV. The elemental analysis of the samples was analyzed by EDS spectra (JEOL Model JED-2300). UV–Vis absorption spectra were taken on a Perkin-Elmer Lambda 2 spectro-meter. Photoluminescence spectra of the samples were recorded using PerkinElmer LS 55 spectrometer equipped with a He–Cd laser source, Excitation length used was 325 nm. The functional groups were

analyzed by using Fourier transformed infrared spectra (FT-IR), which is collected using a 5DX FTIR spectrometer. The composition and chemical state of the final products were analyzed by X-ray photoelectron spectroscopy (XPS) using an ESCALAB-MKII spectrometer (UK) with Al  $K\alpha$  radiation (1486.6 eV) as the X-ray source for excitation.

### 2.4 Photocatalytic setup

A specially designed photocatalytic reactor system made of double walled reaction chamber of glass tubes was used for photodegradation experiments. A 300 W xenon lamp as the light source and the control of the reaction bottle of the plane window 20 cm from the xenon lamp, the reaction using 420 nm high pass filter to remove the ultraviolet light. The photocatalytic degradation reactions of MB and RhB were considered from the model pollutants. The 50 mg of the prepared photocatalyst was mixed with 50 ml of aqueous solution containing the appropriate dye (10 mg/l for MB and RhB). Prior to reactions, the dye solution with catalysts was stirred in the dark for 30 min to attain the adsorption, desorption equilibrium. The concentration of the aqueous suspensions (MB and RhB) in each sample was analyzed using UV–Vis spectrophotometer at a wavelength of  $\lambda_{\text{max}}$ . The degradation efficiency of the dye solution was calculated using the formula

$$\text{Degradation efficiency (\%)} = 1 - (C_t/C_0) \times 100$$

where  $C_0$  and  $C_t$  are initial and final concentration of the dye solutions. The time interval of irradiation time was 20 min.

## 3 Results and discussion

### 3.1 XRD analysis

The crystallography nature and average grain size of the nanoparticles were analyzed through powder XRD method. Figure 1a shows the powder XRD pattern of pure and Sm doped CdS nanoparticles with different Sm content. This PXRD pattern confirms the CdS in the form of face-centered cubic structure and its corresponding diffraction peaks of  $2\theta = 26.57^\circ$ ,  $44.67^\circ$  and  $54.61^\circ$  can be assigned to the (111), (220) and (311) planes of CdS respectively. These results are matched well with the standard value (JCPDS Card No. 80-0019). No other impurity phases were detected in the spectrum. The absence of peaks other than CdS confirms the purity of the sample. These results further indicate that the dopant  $\text{Sm}^{3+}$  ions are incorporated into lattice of CdS nanocrystals. Moreover, the calculated lattice parameters and volume was increases with the increase of Sm content (Table 1). This could be attributed to similar ionic radius of  $\text{Sm}^{3+}$  (0.967 Å) ions in  $\text{Cd}^{2+}$  (0.957 Å). The peak positions

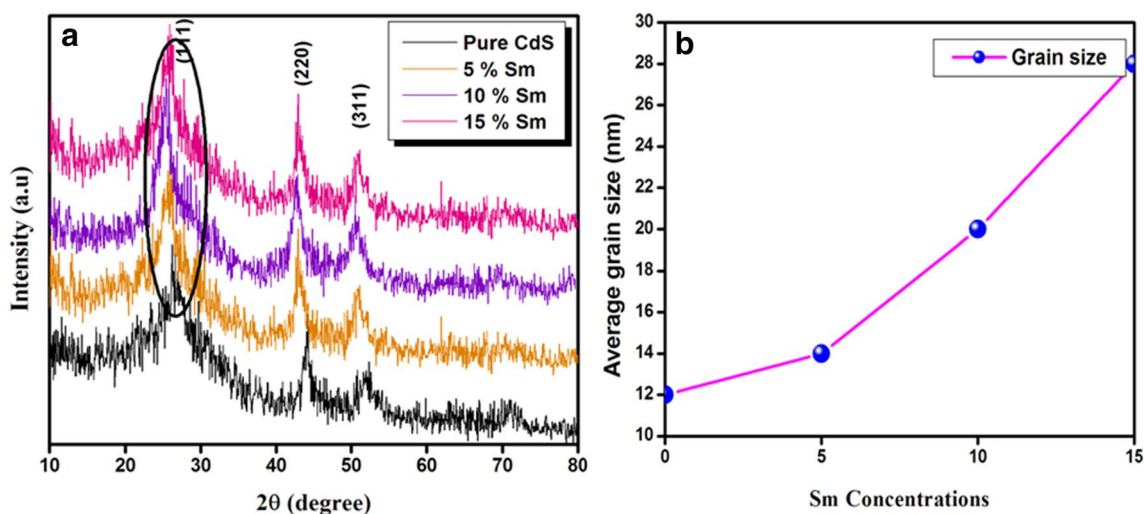


**Fig. 1** a Powder XRD pattern of pure and Sm doped CdS nanoparticles, b variation grain size as a function of Sm content

**Table 1** Shows the grain size, lattice parameter, volume and band gap of pure and Sm doped CdS nanoparticles with different Sm concentrations

Sm concentrations (mol%)	Grain size (nm)	Lattice parameter a (Å)	Volume (Å <sup>3</sup> )	Band gap (eV)
0	12	5.8398	198.99	2.55
5	14	5.8402	199.10	2.47
10	20	5.8455	199.58	2.38
15	28	5.8492	199.89	2.23

in an XRD pattern are related to the lattice parameters. The shift in XRD peaks is surely a result of change in the lattice parameters. In our case after doping Sm the peak intensity was enhanced and shifted towards the lower angle side. This could be due to different ionic radius, electronic density and strain gradient of the Sm and Cd atoms. However, with the increasing of Sm content in the precursors, the peak intensity of these samples became stronger gradually, suggesting these samples tend to be well crystallized. Prasanth et al. [14] have reported Sm doped ZnS nanoparticles using chemical co-precipitation method. They also reported that 15% Sm doped ZnS showed high optical and luminescence properties that other samples (5 and 10 wt%), which is confirmed through UV and PL results. Moreover, there is no impurity phases were detected in the XRD pattern even doped with higher percentage of Sm (15%). This may be due to similar smaller ionic radius of Sm<sup>3+</sup> (0.967 Å) ions than Cd<sup>2+</sup> (0.9823 Å). The same findings were observed in our case (Sm doped CdS). The grain size has been calculated using the Scherrer's formula [15] and found to be 12, 14, 20, 28 nm for pure and Sm (5, 10 and 15 mol%) doped CdS respectively. For clear understanding, we have plotted the

graph between average grain size and Sm content (Fig. 1b). We have similar findings were observed at Sm and Nd doped CdS nanoparticles by synthesized through the chemical co-precipitation method [16].

### 3.2 TEM with EDS analysis

The surface morphology and size of the nanoparticles were analyzed by using TEM images. Figure 2a–c shows the TEM images of pure and Sm (5 and 15 mol%) doped CdS respectively. It was clear evident that both pure and Sm doped CdS consist of very fine particles to form clusters. It was also noted that spherical nanocrystals have formed with very slight aggregation with the increase of Sm content. Fig. 2d show the HRTEM image of 15 mol% doped Sm doped CdS sample, clearly displays lattice fringes, indicating good crystallinity with well connectivity in the nanocrystals. The calculated average particle sizes were around 15–25 nm. In addition that, HRTEM image exhibits three different lattice fringes, which correspond to the (111), (220), and (311) planes of cubic CdS, respectively. The cubic structure with above mentioned planes was also confirmed by XRD results. SAED pattern in the inset of Fig. 2d indicates the corresponding 'halo' ring pattern of cubic phase CdS with polycrystalline nature. The elemental composition of the Sm (15 mol%) doped CdS nanocrystals determined by EDX shown in Fig. 2e. The sample exhibiting only presence of three elements for cadmium, sulfur and samarium peaks. Its corresponding weight and atomic percentage are given in the table (Fig. 2e inset). Therefore, the EDX results again supported that Sm is incorporated into CdS, which is also agreeing with the XRD and TEM results. The Cu element was found in the composition, due to the grid used to for EDS measurements.

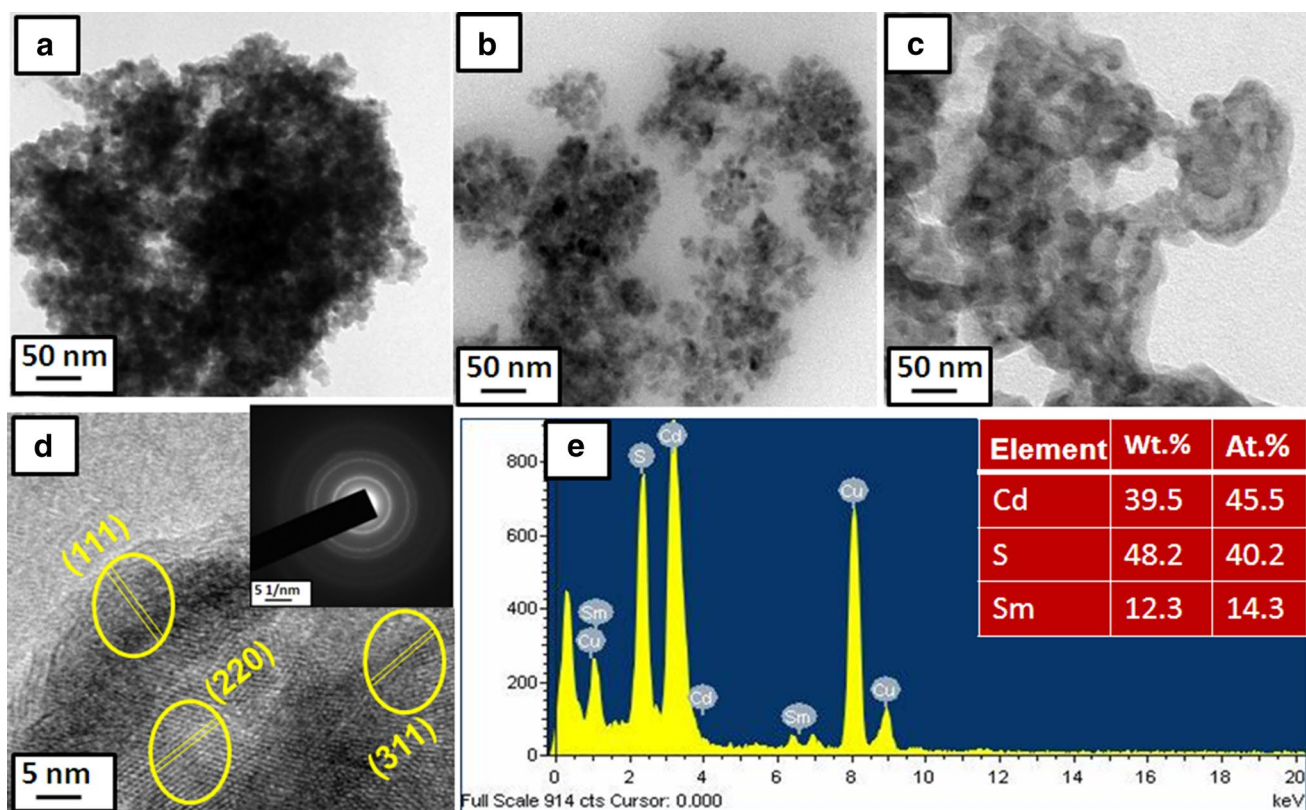


**Fig. 2** TEM images of **a** pure CdS, **b** 10% Sm, **c** 15% Sm, **d** corresponding HRTEM and SAED pattern (inset), **e** EDS spectra of 15% Sm doped CdS nanoparticles

### 3.3 XPS analysis

XPS is a surface analytical technique that can provide useful information on the complete chemical composition of the sample surface. Figure 3 gives XPS profile of 15 mol% Sm doped CdS. Different elements present in the compound are showed in the survey spectrum (Fig. 3a). The constituent's peaks were identified to be cadmium (Cd), sulfur (S), and samarium (Sm). In order get the more detail about the valance state and the chemical composition of Cd, S and Sm, high-resolution spectra were analyzed, as shown in Fig. 3b–d. In Fig. 3b, the Cd 3d levels peaks appeared at 404.91 and 411.65 eV, which is characteristics peak of Cd 3d<sub>5/2</sub> and Cd 3d<sub>3/2</sub>, respectively. The S 2p levels of CdS spectra were shown in Fig. 3c. It can be noted that the S 2p peaks were observed at 161.72 eV is attributed to metal sulfide. The binding energy of S 2p at 161.84 eV also agrees well with a binding energy with blue shift compared to the observed S 2p in bulk CdS [17]. The peak at 1085.37 eV in Fig. 3d is attributed to Sm 3d<sub>5/2</sub> observed in Sm<sup>3+</sup>: CdS nanocrystals [18]. Hence, our XPS results further supported that presence of Sm in CdS nanocrystals with +3 in state.

### 3.4 UV–Vis absorption spectra analysis

To investigate the optical absorption properties and band gap energy of the samples, UV–Vis absorption spectra was carried out. Fig. 4a shows the UV–Vis absorption spectra of pure and Sm doped CdS nanoparticles in the range of 300–800 nm was examined. It was noted that, the absorption edge was found as 480 nm for pure CdS, further it was shifted towards the longer wavelength side with the increase of Sm content. Especially for 15% doped CdS sample had larger absorption ability, which had an obvious doping level in its spectrum since there was a weak peak around 550 nm. For a crystalline semiconducting nanoparticle, it is known that the relationship between optical absorption and band edge is given by the following equation:

$$(\alpha h\nu) = A (\alpha h\nu - E_g)^{n/2}$$

where  $\alpha$ ,  $n$ ,  $E_g$ , and  $A$  are the absorption coefficient, light frequency, bandgap and constant respectively [19]. The optical band gap decreases from 2.55 to 2.23 eV with increasing Sm concentration (Fig. 4b). The decrease in band gap energy can be attributed to 15% Sm doped CdS have greater

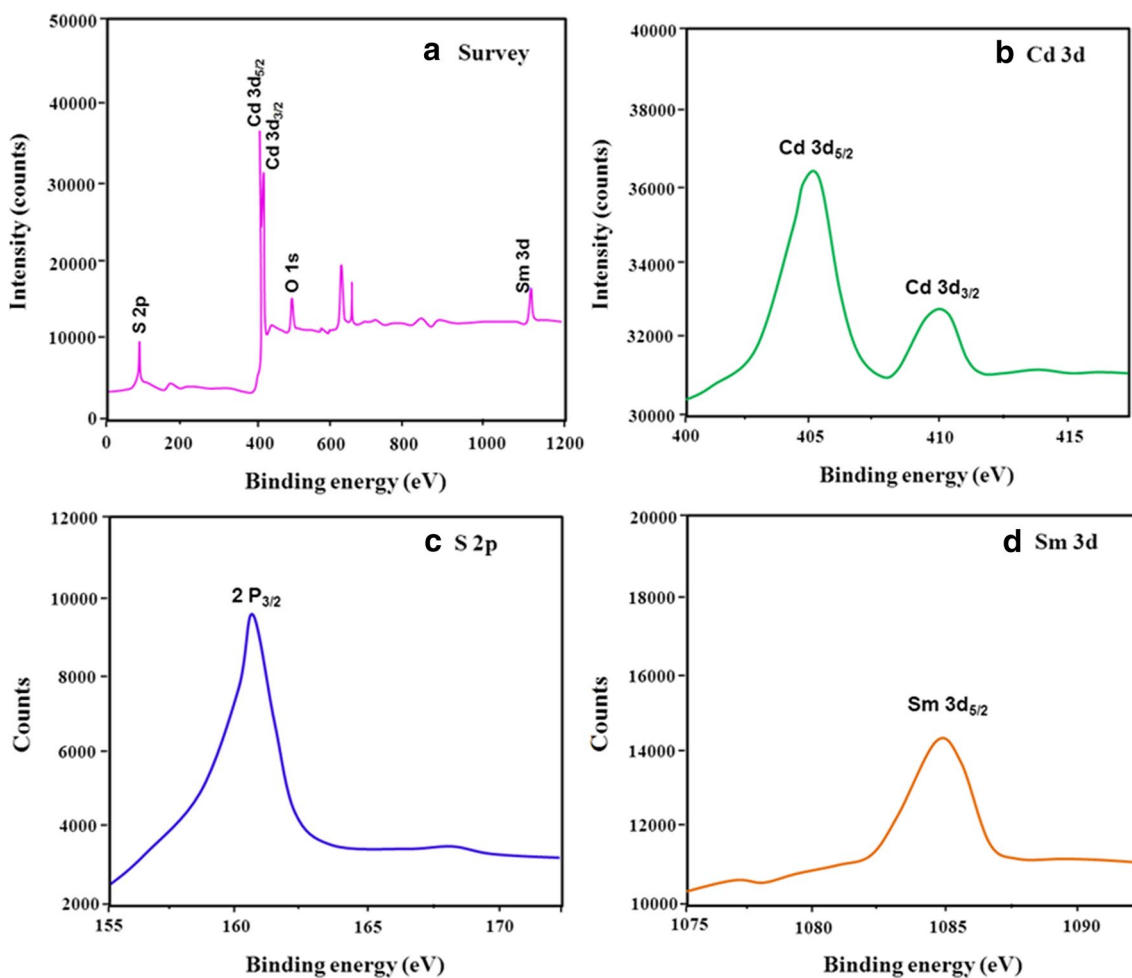


Fig. 3 XPS spectra for a a survey spectrum of 15% Sm doped CdS, b Cd 3d, c S 2p, and d Sm 3d

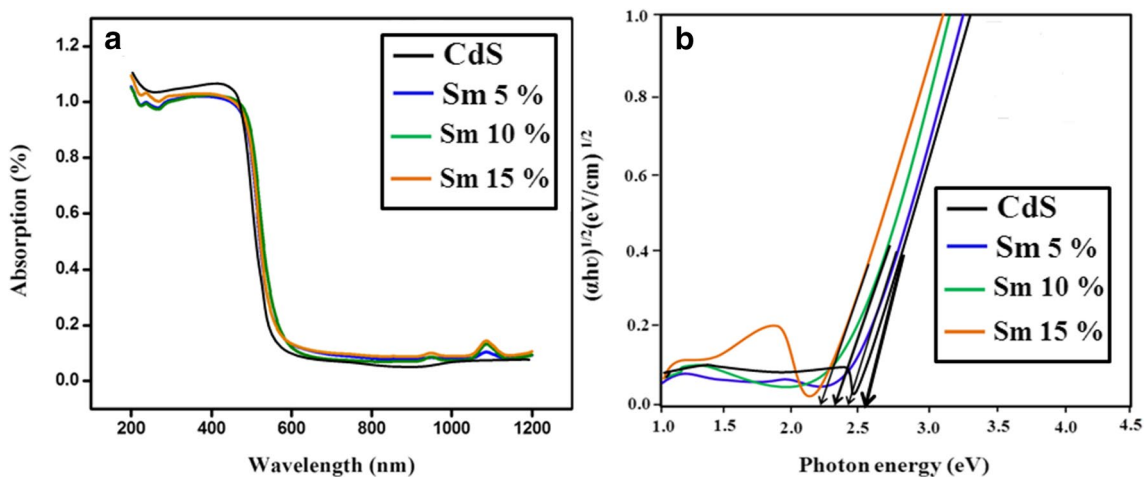
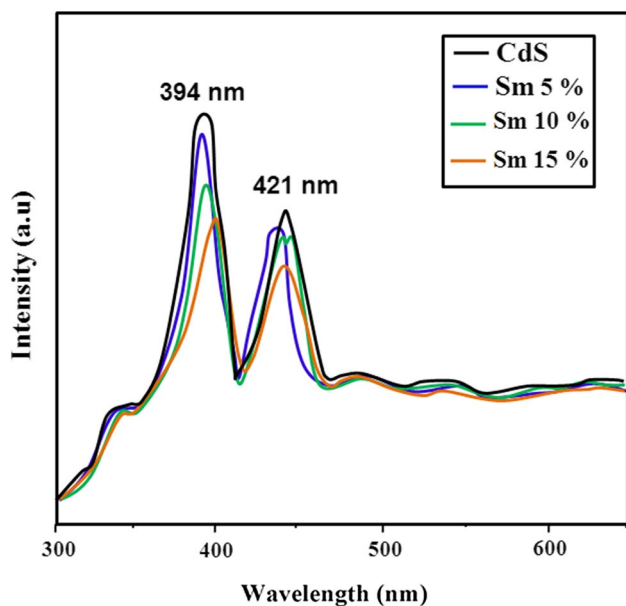


Fig. 4 a UV-Vis absorptions spectra of pure and Sm doped CdS nanoparticles, b band-gap determination

carrier concentration, since the optical absorption in this wavelength region is due to free-carrier absorption of the conduction electrons. Thus it is speculated that this sample may have the highest visible-light driven photocatalytic activity. Similarly Agrawal et al. stated that, increasing La concentrations on CdS–Se films shifts the emission spectra towards a longer wavelength, which is caused due to the transfer of energy from energy levels of La ion [20].

### 3.5 Photoluminescence spectra analysis

Photoluminescence (PL) studies of the materials provided a comprehensive knowledge about the localized defect states such as vacancies and interstitials; which act as trapping and recombination centers across the band gap of semiconductor nanoparticles. Figure 5 shows the room temperature photoluminescence spectra of pure and Sm doped CdS nanoparticles in the range from 300 to 600 nm excitation wavelength. It was shown that the emission spectra for all the samples illustrate a band-edge emission at 394 nm. It was reported that this kind of band-edge luminescence can be caused by the recombination of excitons and/or shallowly trapped electron–hole pairs [21, 22]. The next weak emission appeared at 420 nm is attributed to the emission of surface states due to the small size of nanocrystals. The luminescence emissions (394 and 420 nm) spectra of the both pure  $\text{Sm}^{3+}$  doped CdS nanoparticles is generally due to transition of  $^5\text{D}_0 \rightarrow ^7\text{F}_2$  and  $^5\text{D}_0 \rightarrow ^7\text{F}_1$  respectively. With increasing concentration of  $\text{Sm}^{3+}$  ions, the peaks get shifted towards longer wavelength, which is due to



**Fig. 5** Room temperature photoluminescence spectra of pure and Sm doped CdS nanoparticles

the energy transfer from energy levels of Sm ion. When a higher percentage of Sm is doped into the CdS crystal lattice, changes in the band gap and lattice distortions are expected to enhance the red shift in the emission spectra. The clear red-shift in the absorption edge was also confirmed by UV–Vis absorption spectra.

### 3.6 FTIR spectra analysis

FTIR spectroscopy can be used to estimate the nature of surface of nanostructure materials. To derive the surface structure of pure and Sm doped CdS based nanostructure, we carried out FTIR measurement in the wavenumber range from 400 to 4000  $\text{cm}^{-1}$  using the KBr method at room temperature shown in Fig. 6. The broad band ranging from 3300 to 3600  $\text{cm}^{-1}$  centered at 3420.57  $\text{cm}^{-1}$  and a weak band at 1634.15  $\text{cm}^{-1}$  is due to stretching and bending vibration of O–H group respectively [23]. In general, Cd–S bond stretch vibration appeared below 700  $\text{cm}^{-1}$ , hence the strong peak located at 631.57 in present case can be assigned for Cd–S stretch vibration [24]. There is no peak evidence related to Sm–O band vibrations in the spectra, which again supported that substitution of  $\text{Sm}^{3+}$  ions in the CdS nanocrystal.

### 3.7 Photocatalytic studies

#### 3.7.1 Absorbance and visible light driven photocatalytic test

MB dye is a heterocyclic aromatic chemical compound with molecular formula  $\text{C}_{16}\text{H}_{18}\text{C}_1\text{N}_3\text{S}$ . It is a solid odorless, dark green powder that yields a blue solution when

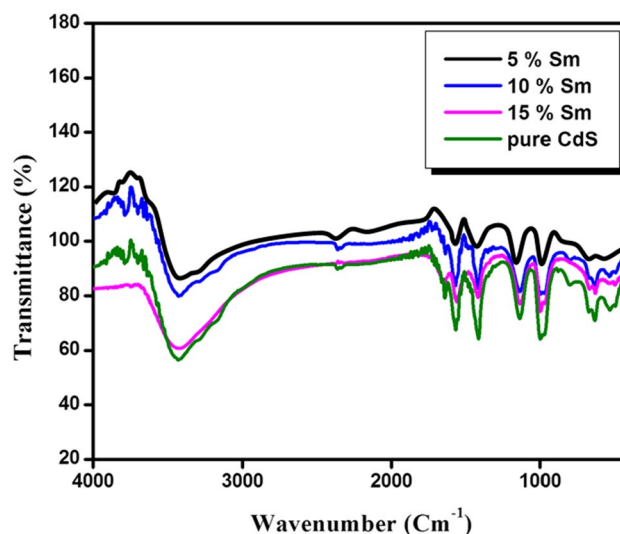


**Fig. 6** FTIR spectra of pure and Sm doped CdS nanoparticles

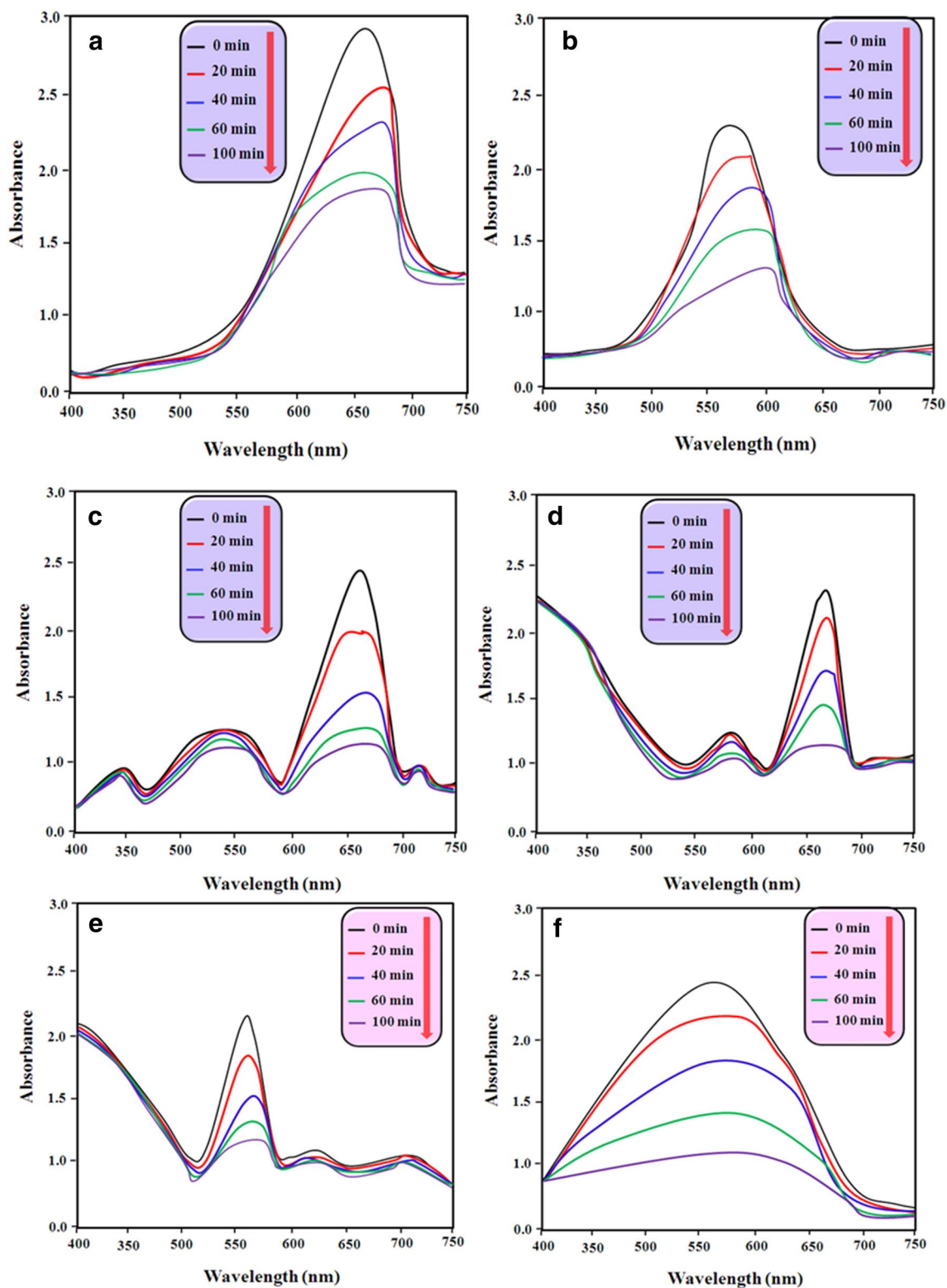


**Fig. 7** UV absorption spectra of MB dye solution by using **a** pure CdS, **b** 5% Sm and **c** 15% Sm doped CdS nanoparticles; UV absorption spectra of RhB dye solution by using **d** pure CdS, **e** 5% Sm and **f** 15% Sm doped CdS nanoparticles under visible light irradiation

dissolved in water at room temperature. The dye has a problem of disposal due to its high solubility in water. Traces of this dye are also harmful for the environment. In view of the above, the degradation of MB dye has been studied in the present study with RhB under UV light irradiation. The effect of the Sm doped CdS catalyst material was examined by monitoring the intensity of absorption and emission peaks with irradiation time. The absorption spectra of the aqueous solution of MB and RhB dyes irradiated under visible light are recorded at the time interval of 20 min and shown in Fig. 7a–f. The peak maximum for the absorbance spectra of MB (at 665 nm) and RhB (at 554 nm) decreases gradually with increasing irradiation time, allowing quantification of the photocatalytic discoloration of MB and RhB. The color of the solutions like dark blue and pink was turned to light blue and pink color of MB and RhB dye solutions respectively. The samples further tested for degradation efficiency under visible light irradiation with a regular interval of 20 min and the corresponding temporal graph was shown in Figs. 8 and 9. It is also found that the 15 mol% Sm-doped CdS nanoparticles demonstrated highest activity in the series of Sm-doped CdS photocatalysts. After 100 min of visible light irradiation, the MB degradation efficiency was found to be 55, 68, 85 and 94% for pure and Sm 5, 10 and 15 mol% doped CdS respectively. Similarly, the RhB removal efficiency was found to be 62, 72, 89 and 98% for pure and Sm 5, 10 and 15 mol% doped CdS respectively. This result indicates that Sm (15%)-doped CdS has higher photocatalytic activity than other Sm-doped CdS for MB and RhB degradation. An appropriate amount of Sm can form the surface chemical groups, such as O–H, which can be found in Fig. 6 (FTIR spectra). Due to the strong electron-withdrawing

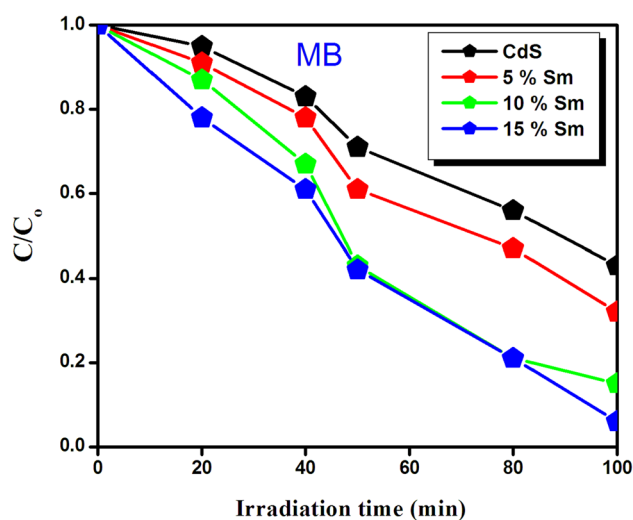


**Fig. 8** Temporal degradation profile of MB using pure and Sm doped CdS catalyst under visible light irradiation

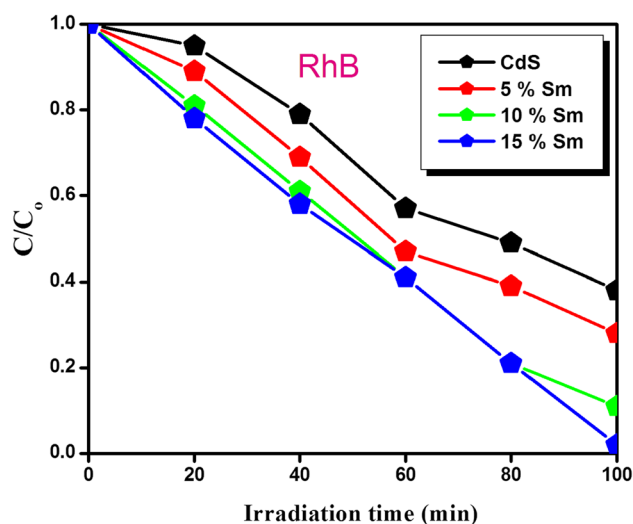


**Fig. 9** Temporal degradation profile of RhB using pure and Sm doped CdS catalyst under visible light irradiation

property of these groups, hydroxyl can accelerate the photocatalytic process of CdS nanocatalyst and improve its photocatalytic efficiency. This could be attributed to the  $\text{Sm}^{3+}$  doping can provide them with exciting properties inherited from the synergetic effect. We can find that the activity of Sm-doped CdS is enhanced monotonously with the  $\text{Sm}^{3+}$  content increasing. This can be partly attributed to the relatively high doping concentrations of  $\text{Sm}^{3+}$ , which might cause an increased adsorption of both MB and RhB and become the recombination center of photogenerated carriers, resulting in a increase of photocatalytic efficiency. When  $\text{Cd}^{2+}$  ions are replaced by  $\text{Sm}^{3+}$  ions more hydroxide ions are adsorbed on the cadmium surface, these excess hydroxide ions are acting as hole trapping agents, which delay electron–hole recombination reaction and hence enhances the photocatalytic activity. In addition, inhibition of the  $e^-/h^+$  recombination and the increase in the absorption of visible light of Sm doped CdS is another important factor. This is also explained in PL spectra analysis. Arasi et al. [25] have synthesized Sm doped CdS nanoparticles using one step hydrothermal method and studied the photocatalytic properties of RhB. The degradation efficiency was found to be 95%. Ertis et al. [26] have reported photocatalytic activity of methylene blue using Sb doped CdS catalyst under visible light irradiation. They observed only 84% degradation efficiency of MB by Sm doped CdS catalyst. Luo et al. [27] have reported Ni doped CdS catalyst towards degradation of RhB under visible light. They also found only 95% degradation efficiency of RhB. Compared with the above results, our newly prepared Sm doped CdS catalyst showed highest photocatalytic behavior towards MB and RhB under visible light irradiation.

### 3.7.2 Recycle test

In order to test the stability of the pure and Sm-doped CdS, we reused the catalyst for seven recycles by MB and RhB degradation under visible light irradiation. Figures 10 and 11 show the recycle test of pure and Sm doped CdS catalyst under visible light irradiation. As shown in Figs. 10 and 11a, b, the catalyst could be reused seven times without significant deactivation after seven times recycling. The results showed that after seven cycles, only small variation was observed in the photocatalytic efficiency, this could be due to incomplete recollection and loss during the washing process. The results suggest that Sm doped CdS catalyst showed good stability and recyclability. Hence, this type of catalyst powders might be a promising potential application in high performance photocatalytic device.

### 3.7.3 Photocatalytic mechanism

The schematic representation of photocatalytic mechanism of Sm–CdS under visible light is shown in Fig. 10c. The photocatalytic reaction generally includes photoexcitation, charge separation and migration, and surface oxidation–reduction reactions. The reactive species generated during illumination of photocatalysts are  $h^+$ ,  $OH^-$ , and  $\cdot O_2^-$ . To understand the mechanism of Sm doped CdS for degradation dyes, it is necessary to detect which reactive species plays a major role in the photocatalytic degradation process. During the photodegradation of dyes over Sm doped CdS, the  $h^+$ ,  $\cdot OH$ , and  $O_2^-$  are eliminated into the reaction solution, respectively. When the presence of visible light absorbed efficiently by both Sm–CdS catalyst and the dye molecules (MB and RhB), electrons in the valence band of Sm–CdS could be excited to the conduction band

and electron–hole pairs are generated. On the other hand, visible-light irradiation can excite the VB electrons of CdS to the Fermi level ( $E_F$ ) of Sm (formation of the hole ( $h_{vb}^+$ ) in VB of CdS), which following reaction of the hole with water can also create  $OH^-$  radicals. These radicals are highly reactive, and reaction of them finally degradation of the organic pollutants [28]. Then the molecular oxygen ( $O_2$ ) near the boundary photocatalyst could be rapidly condensed to the superoxide radical ( $O_2^-$ ) and hydrogen peroxide radical ( $\cdot OOH$ ) by the photogenerated electrons, while the valence band holes can directly oxidize organic pollutants adsorbed on the surface of catalyst (Sm–CdS) or mineralized them indirectly through hydroxyl radicals ( $\cdot OH$  generated by the reaction of holes and water molecules ( $H_2O$ ) or chemisorbed ( $OH^-$ )). When the presence of visible light irradiation energy exceeds the energy difference between the valence and conduction bands (band gap) of a semiconductor, electron–hole pairs will be generated. This is referred to as the photoexcited state of the semiconductor. The photogenerated charges (i.e.,  $e^-$  and  $h^+$  carriers) cause oxidation reactions on the particle surface, giving rise to free radicals, which in turn degrade the organic molecules. Finally, these  $OH^-$  radicals having a strong oxidation power, can lead to a partial or complete mineralization of the organic substances (MB and RhB) in the waste water, forming non-toxic products such as  $CO_2$  and  $H_2O$ . ( $OH^- + \text{pollutants} \rightarrow \text{Intermediated products} \rightarrow CO_2, H_2O$ ). In our case, the higher concentration of Sm (15%) is higher photocatalytic activity than other concentration of Sm (5 and 10%) doped CdS. This could be attributed to tuning of band gap and particle size of the CdS nanocrystals, which enhance the more absorption visible light properties and increasing the photocatalytic efficiency.

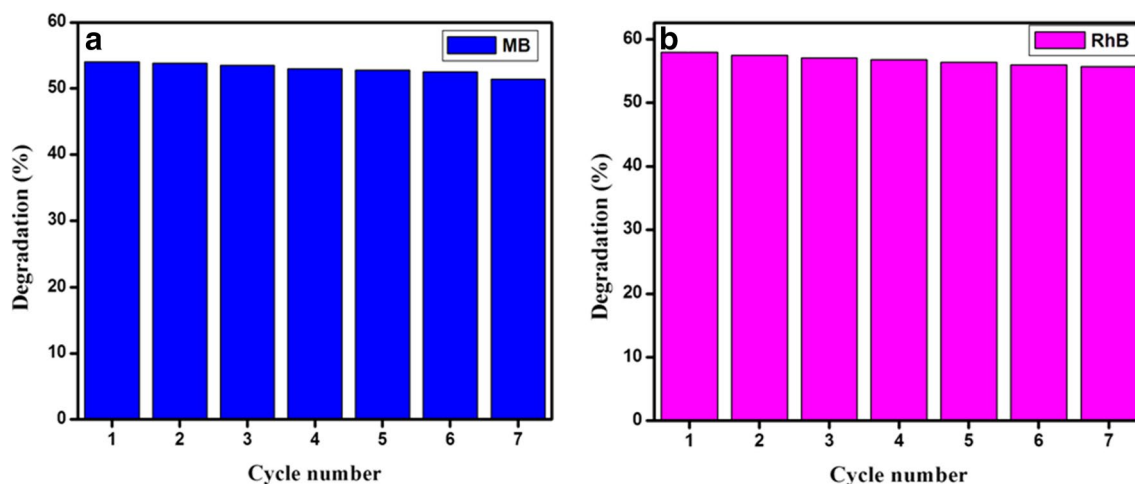
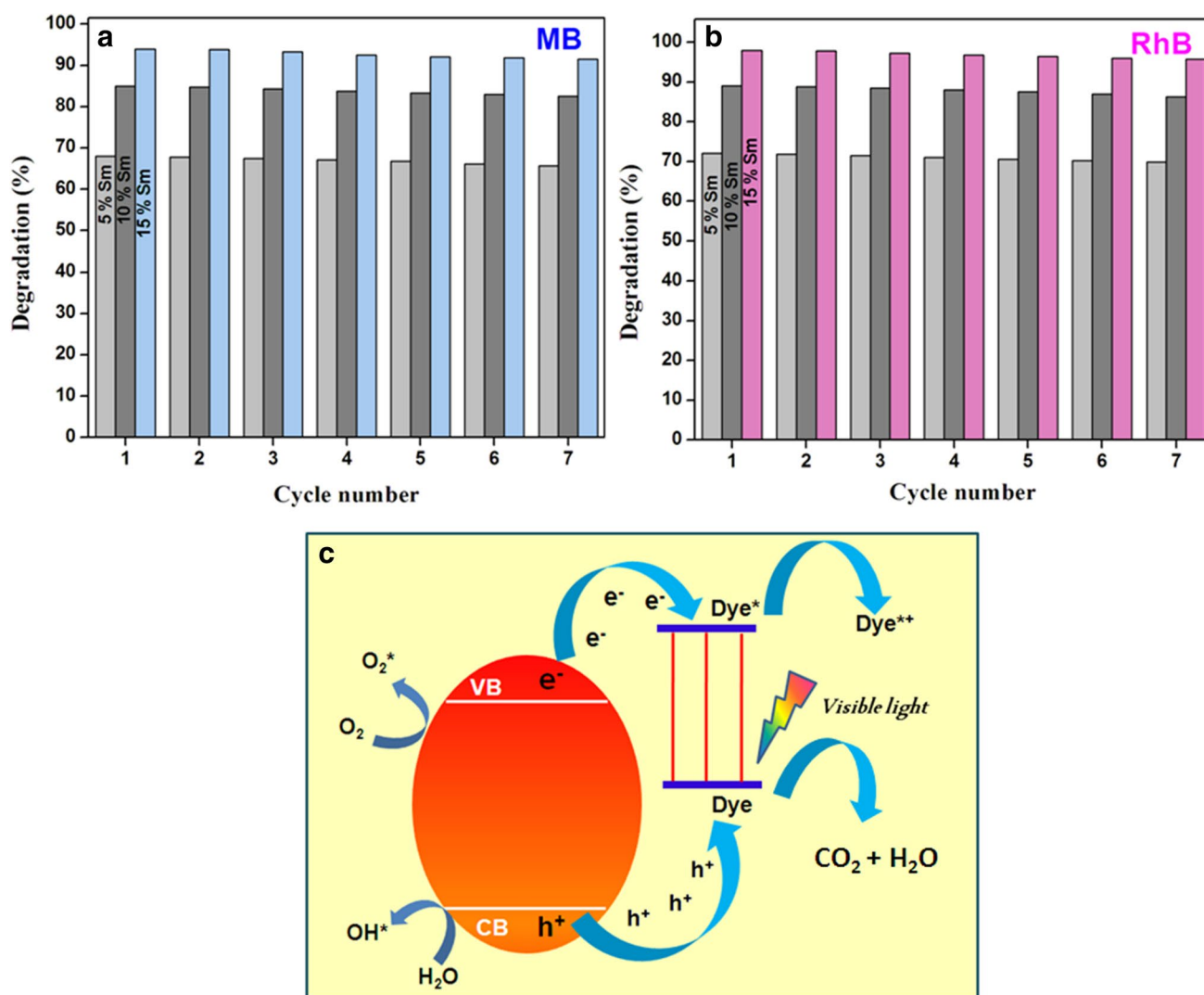


Fig. 10 Recycling cycles of test of pure CdS catalyst under visible light irradiation **a** MB and **b** RhB



**Fig. 11** Recycling cycles of test of **a** MB, **b** RhB using pure and Sm doped CdS catalyst under visible light irradiation and **c** schematic representation for photocatalytic mechanism of Sm doped CdS catalyst under visible light irradiation

## 4 Conclusion

In summary, Sm-doped CdS nanoparticles were prepared by simple wet chemical route. The formation of CdS and Sm-doping was confirmed by PXRD and EDX spectrum. TEM micrograph revealed that the Sm-doped CdS have spherical shape nanoparticles. After doping, the change in the morphology was not observed in the present work. The XPS spectrum confirms that presence of Sm was  $3^+$  in state. Optical properties were enhanced by increasing the concentration of Sm doping up to 15 mol%. The alteration of Sm into CdS catalyst shows higher adsorption with synergistic effect and enhances the separation of photogenerated electron-hole pairs, important to higher photocatalytic degradation efficiency. The Sm doped CdS may have the potential for environmental purifications in future.

## References

1. P. Roy, S. Berger, P. Schmuki, TiO<sub>2</sub> nanotubes: synthesis and applications. *Angew. Chem. Int. Ed.* **50**, 2904–2939 (2011)
2. S. Liu, J. Yu, M. Jaroniec, Tunable photocatalytic selectivity of hollow TiO<sub>2</sub> microspheres composed of anatase polyhedra with exposed {001} facets. *J. Am. Chem. Soc.* **132**, 11914–11916 (2010)
3. X.H. Li, J.S. Zhang, X.F. Chen, A. Fischer, A. Thomas, M. Antonietti, X.C. Wang, Condensed graphitic carbon nitride nanorods by nanoconfinement: promotion of crystallinity on photocatalytic conversion. *Chem. Mater.* **23**, 4344–4348 (2011)
4. Y.B. Chen, L.Z. Wang, G.Q. Lu, X.D. Yao, L. Guo, Nanoparticles enwrapped with nanotubes: a unique architecture of CdS/titanate nanotubes for efficient photocatalytic hydrogen production from water. *J. Mater. Chem.* **21**, 5134–5141 (2011)
5. G. Liu, J.C. Yu, G.Q. Lu, H.M. Cheng, Crystal facet engineering of semiconductor photocatalysts: motivations, advances and unique properties. *Chem. Commun.* **47**, 6763–6783 (2011)

- T.F. Zhou, J.C. Hu, J.L. Li, Er<sup>3+</sup> doped bismuth molybdate nanosheets with exposed {010} facets and enhanced photocatalytic performance. *Appl. Catal. B* **110**, 221–230 (2011)
- J.Y. Xiong, G. Cheng, Z. Lu, J.L. Tang, X.L. Yu, R. Chen, BiO-COOH hierarchical nanostructures: shape-controlled solvothermal synthesis and photocatalytic degradation performances. *CrystEngComm* **13**, 2381–2390 (2011)
- M. Ibáñez, J.D. Fan, W.H. Li, D. Cadavid, R. Nafria, A. Carrete, A. Cabot, Means and limits of control of the shell parameters in hollow nanoparticles obtained by the Kirkendall effect. *Chem. Mater.* **23**, 3095–3104 (2011)
- Z.Y. Liu, H.W. Bai, D. Sun, Facile fabrication of hierarchical porous TiO<sub>2</sub> hollow microspheres with high photocatalytic activity for water purification. *Appl. Catal. B* **104**, 234–238 (2011)
- S.D. Wu, Z.G. Zhu, Z.P. Zhang, L. Zhang, Preparation of the CdS semiconductor nanofibril by UV irradiation. *Mater. Sci. Eng. B* **90**, 206–208 (2002)
- W.S. Chang, C.C. Wu, M.S. Jeng, K.W. Cheng, C.M. Huang, T.C. Lee, Ternary Ag–In–S polycrystalline films deposited using chemical bath deposition for photoelectrochemical applications. *Mater. Chem. Phys.* **120**, 307–312 (2010)
- Q. Xiao, Z. Si, Z. Yu, G. Qiu, Sol–gel auto-combustion synthesis of samarium-doped TiO<sub>2</sub> nanoparticles and their photocatalytic activity under visible light irradiation. *Mater. Sci. Eng. B* **137**, 189–194 (2007)
- J.C. Sin, S.M. Lam, K.T. Lee, A.R. Mohamed, Photocatalytic performance of novel samarium-doped spherical-like ZnO hierarchical nanostructures under visible light irradiation for 2,4-dichlorophenol degradation. *J. Colloid Interface Sci.* **401**, 40–49 (2013)
- S. Prasanth, P. Irshad, D.R. Raj, T.V. Vineeshkumar, R. Philip, C. Sudarsanakumar, Nonlinear optical property and fluorescence quenching behavior of PVP capped ZnS nanoparticles co-doped with Mn<sup>2+</sup> and Sm<sup>3+</sup>. *J. Lumin.* **166**, 167–175 (2015)
- M. Parthibavarman, V. Hariharan, C. Sekar, V.N. Singh, Effect of copper on structural, optical and electrochemical properties of SnO<sub>2</sub> nanoparticles. *J. Optoelectron. Adv. Mater.* **12**, 1894–1898 (2010)
- L. Saravanan, R. Jayavel, A. Pandurangan, L. Jih-Hsin, M. Hsin-Yuan, Synthesis, structural and optical properties of Sm<sup>3+</sup> and Nd<sup>3+</sup> doped cadmium sulfide nanocrystals. *Mater. Res. Bull.* **52**, 128–133 (2014)
- U. Winkler, D. Eich, Z.H. Chen, R. Fink, S.K. Kulkarni, E. Umbach, Detailed investigation of CdS nanoparticle surfaces by high resolution photoelectron spectroscopy. *Chem. Phys. Lett.* **306**, 95–102 (1999)
- H.R. Hoekstra, Phase relationships in the rare earth sesquioxides at high pressure. *Inorg. Chem.* **5**, 754–757 (1966)
- N. Ghobadi, Band gap determination using absorption spectrum fitting procedure. *Int. Nano Lett.* **3**, 1–4 (2013)
- S. Agrawal, A. Khare, Effect of La on optical and structural properties of CdS–Se films. *Arab. J. Chem.* **8**, 450–455 (2011)
- G.Z. Wang, W. Chen, C.H. Liang, Y.W. Wang, G.W. Meng, L.D. Zhang, Preparation and characterization of CdS nanoparticles by ultrasonic irradiation. *Inorg. Chem. Commun.* **4**, 208–210 (2001)
- W.Z. Wang, Y. Geng, P. Yan, F.Y. Liu, Y. Xie, Y.T. Qian, Synthesis and characterization of MSe (M = Zn, Cd) nanorods by a new solvothermal method. *Inorg. Chem. Commun.* **2**, 83–85 (1999)
- A.K. Singh, G.S. Thool, P.R. Bangal, S.S. Madhavendra, S.P. Singh, Low temperature Mn doped ZnO nanorod array: synthesis and its photoluminescence behavior. *Ind. Eng. Chem. Res.* **53**, 9383–9290 (2014)
- S. Li, L. Zhang, T. Jiang, L. Chen, Y. Lin, D. Wang, T. Xie, Construction of shallow surface states through light Ni doping for high-efficiency photocatalytic hydrogen production of CdS nanocrystals. *Chem. Eur. J.* **20**, 311–316 (2014)
- S.E. Arasi, J. Madhavan, M.V. Antony Raj, Effect of samarium (Sm<sup>3+</sup>) doping on structural, optical properties and photocatalytic activity of titanium dioxide nanoparticles. *J. Taibah Univ. Sci.* **12**, 186–190 (2018)
- I.F. Ertis, I. Boz, Synthesis and optical properties of Sb-doped CdS photocatalysts and their use in methylene blue (MB) degradation. *Int. J. Chem. React. Eng.* **15**, 12–21 (2016)
- M. Luo, Y. Liu, J. Hu, H. Liu, J. Li, One-pot synthesis of CdS and Ni-doped CdS hollow spheres with enhanced photocatalytic activity and durability. *ACS Appl. Mater. Interfaces* **4**, 1813–1821 (2012)
- A.H. Keihan, H. Rasoulnezhad, A. Mohammadgholi, S. Sajjadi, R. Hosseinzadeh, M. Farhadian, G. Hosseinzadeh, Pd nanoparticle loaded TiO<sub>2</sub> semiconductor for photocatalytic degradation of Paraoxon pesticide under visible-light irradiation. *J. Mater. Sci.: Mater. Electron.* **28**, 16718–16727 (2017)